

AFRL Contributions to the Third International Workshop on High-Order CFD Methods

Daniel J. Garmann and Miguel R. Visbal
Air Force Research Laboratory, Wright-Patterson AFB, OH 45433

Code Description

All simulations were performed with the extensively validated high-order, Navier-Stokes solver, FDL3DI^{1;2}. In this code, a finite-difference approach is employed to discretize the governing equations, and all spatial derivatives are obtained with high-order compact-differencing schemes.³ At boundary points, higher-order one sided formulas are utilized that retain the tridiagonal form of the scheme^{1;2}. The derivatives of the inviscid fluxes are obtained by forming the fluxes at the nodes and differentiating each component with the compact differencing scheme. Viscous terms are obtained by first computing the derivatives of the primitive variables. The components of the viscous fluxes are then constructed at each node and differentiated by a second application of the same scheme. In the case of a maneuvering wing, the grid is moved in a rigid fashion using the prescribed kinematics. The time metric terms are evaluated employing the procedures described in detail in Ref. 4 to ensure that the geometric conservation law (GCL) is satisfied.

In order to eliminate spurious components of the solution, a high-order, low-pass spatial filtering technique^{1;5} is incorporated that is based on templates proposed in References 3 and 6. With proper choice of coefficients, it provides a $2N^{\text{th}}$ -order formula on a $2N + 1$ point stencil. These coefficients, along with representative filter transfer functions, can be found in References 2 and 5. The filter is applied to the conserved variables along each transformed coordinate direction one time after each time step or sub-iteration. For the near-boundary points, the filtering strategies described in References 1 and 5 are used. For transitional and turbulent flows, the high-fidelity spatial algorithmic components provide an effective implicit LES approach in lieu of traditional SGS models, as demonstrated in References 7 and 8 and more recently in Ref. 9. All computations presented here are performed with a sixth-order interior discretization scheme coupled with an eighth-order accurate implicit filter.

Time marching of the governing equations is typically achieved through the iterative, implicit approximately-factored integration method of Beam and Warming¹⁰. This method has been simplified through the diagonalization of Pulliam and Chaussee¹¹ and supplemented with the use of Newton-like sub-iterations to achieve second-order accuracy^{7;8}. Sub-iterations are commonly used to reduce errors due to factorization, linearization, diagonalization, and explicit specification of boundary conditions¹². Fourth-order, nonlinear dissipation terms^{13;14} are also appended to the implicit operator to augment stability. The classical fourth-order, four-stage Runge-Kutta method implemented in the low-storage form described in Ref. 15 is also available within FDL3DI. Explicit time-integration is unsuitable for the wall-bounded flows considered in this work, so cases C2.3 and C3.4 discussed below utilize the implicit, second-order scheme, while case C3.3 employs the Runge-Kutta time advancement.

MPI parallelization is utilized in the code through domain decomposition and overset. Typically, five planes of overlap are maintained between adjacent blocks to provide communication. Periodicity

is also imposed by means of a five-plane overlap that exchanges data after each stage or sub-iteration of the time-advancement procedure. Shared memory parallelization is also implemented through OpenMP directives to allow threading of each MPI task for hybrid parallelization, which has been shown to achieve nearly perfect scalability for thread counts up to 8 or 16, depending on system architecture.

Case Summaries & Results

Several cases have been analyzed. These correspond to the heaving and pitching airfoil (C2.3), DNS of the Taylor-Green Vortex (C3.3), and DNS and LES of flow over 2D periodic hill (C3.4). Each is summarized below accompanied with the respective results.

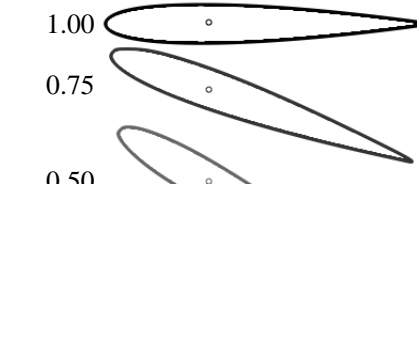
C2.3: Heaving and Pitching Airfoil

Case summary

A NACA0012 airfoil is subjected to a heaving and pitching motion given by

$$h(t) = \begin{cases} 0, & \text{if } t < 0 \\ \frac{1-\cos \pi t}{2}, & \text{if } 0 \leq t < 1 \\ 1, & \text{otherwise} \end{cases}$$

$$\theta(t) = \begin{cases} 0, & \text{if } t < 0 \\ \frac{\pi}{6} \frac{1-\cos \pi t}{2}, & \text{if } 0 \leq t < 1 \\ 1, & \text{otherwise} \end{cases}$$



where t is the solution time, $h(t)$ is the vertical displacement of the airfoil, and $\theta(t)$ is the corresponding angle of attack relative to the free stream and taken about the $1/3$ chord position. The airfoil's trailing edge is rounded ($r/c = 0.0018$) to facilitate an O-grid topology for discretization of the surface. For the baseline (coarse) configuration, 161 gridlines are distributed circumferentially around the airfoil (ξ -direction) with variable spacing ranging from $(\Delta s/c) = 4.0 \times 10^{-3}$ at the leading edge to 8.0×10^{-4} at the trailing edge, while the maximum spacing achieved in between is $(\Delta s/c)_{\max} = 2.0 \times 10^{-2}$. This circumferential distribution is hyperbolically marched away from the surface (η -direction) using 100 gridlines with an initial off-body spacing of $(\Delta n/c)_0 = 4.0 \times 10^{-4}$ that is stretched until reaching a circular far field boundary located 100 chord-lengths from the surface. A depiction of the mesh can be seen in Fig. 1. Two refined meshes (medium and fine) are formed by refining the baseline grid globally by factors of 4 and 16, respectively. The specific sizes and spacings of each mesh are listed in Table 1.

At the far field boundary, free stream conditions are specified. It should be noted that near this boundary, the mesh is stretched quite drastically, which in conduction with the high-order filtering of the ILES scheme, provides a buffer-like region that prevents spurious waves from reflecting into the domain. The airfoil surface is prescribed as a no-slip wall with a zero-normal pressure gradient that is enforced through a fourth-order accurate extrapolation. The free stream Mach number is set as $M_\infty = 0.2$, Prandtl number is $Pr = 0.72$, and two Reynolds numbers are considered: $Re = 1000$ and 5000 .

Table 1: Details of the computational domain for the heaving and pitching airfoil

Mesh	$n_\xi \times n_\eta$	$(\Delta n/c)_0$	$(\Delta s/c)_{LE}$	$(\Delta s/c)_{TE}$	$(\Delta s/c)_{\max}$
Coarse	161×100	4.0×10^{-4}	4.0×10^{-3}	8.0×10^{-4}	2.0×10^{-2}
Medium	320×198	2.0×10^{-4}	2.0×10^{-3}	4.0×10^{-4}	1.0×10^{-2}
Fine	639×395	1.0×10^{-4}	1.0×10^{-3}	2.0×10^{-4}	0.5×10^{-2}

n_ξ, n_η	Circumferential and normal mesh dimensions
$(\Delta n/c)_0$	Initial off-body spacing
$(\Delta s/c)_{LE, TE, \max}$	Leading edge, trailing edge, and maximum streamwise spacings

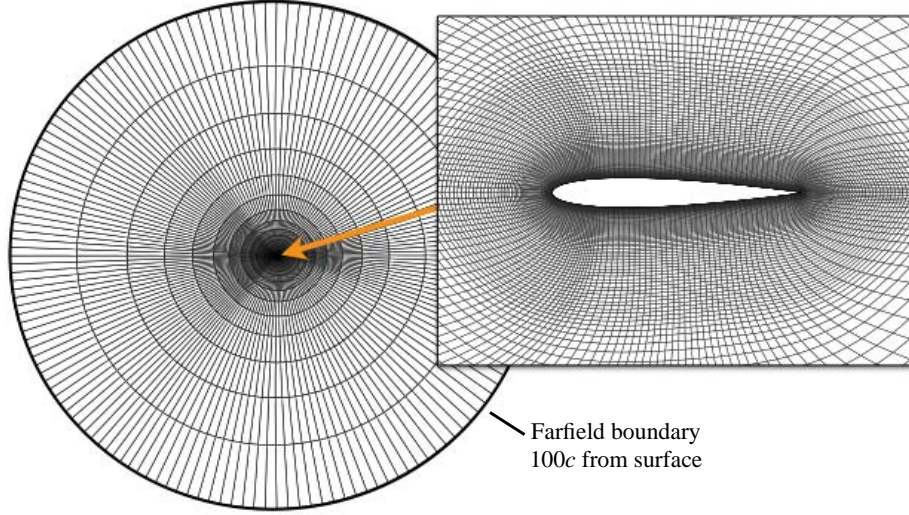


Figure 1: O-grid topology and near-field discretization for the NACA0012 domain at the baseline resolution

Results

Simulations of the heaving and pitching airfoil have been conducted with each mesh and for each time step of $\Delta\tau = (4.00, 2.00, 1.00, 0.50, 0.25) \times 10^{-3}$ to ensure adequate spatial and temporal resolution is achieved for the quantities of interest. The requested metrics for comparison correspond to the work (W) and vertical impulse (I) which the fluid exerts on the airfoil during the motion. These integrated values as given from the case description are

$$W = \int_0^1 [F_y(t) \dot{h}(t) + T_z(t) \dot{\theta}(t)] dt \quad (1)$$

and

$$I = \int_0^1 F_y(t) dt \quad (2)$$

where $F_y(t)$ and $\dot{h}(t)$ are the vertical force and velocity, respectively, and $T_z(t)$ and $\dot{\theta}(t)$ are the torque and angular velocity, respectively, about the 1/3 chord location. Time histories of the integrands (the power and vertical force) are recorded for each time-step and spatial resolution, and trapezoidal integrations are performed as a post-processing step. The corresponding time histories for both Reynolds numbers are presented in Fig. 2 for the fine resolution at a time step of 0.5×10^{-3} .

The work and impulse for all spatial and temporal resolutions are presented in Tables 2 and 3 for $Re = 1000$ and 5000 , respectively. At both Reynolds numbers, a fairly weak sensitivity is seen with spatial resolution as each mesh provides nearly the same result. A stronger but still small variation is seen with temporal refinement indicating that temporal errors mostly dominate the spatial contributions for $\Delta\tau < 0.001$. The integrated quantities are completely converged to the same value (three significant figures) on each mesh for $Re = 1000$ with $\Delta\tau = 0.0005$. The instantaneous flow structure is displayed in Fig. 3 through vorticity contours. It is seen that more than adequate spatial resolution of the near-field flow is provided by the baseline (mesh) at this Reynolds number. Refinement of the mesh does capture a sharper trailing edge vortex into the wake, however, it's far proximity to the airfoil does not significantly affect the integrated quantities on the surface.

At $\text{Re} = 5000$, however, we see that the integrated quantities from the medium and fine resolutions converge to the same value between $\Delta\tau = 0.0005$ and 0.00025 , while the coarse resolution does not quite reach the intended values. The reason for this discrepancy at the coarse resolution can be seen in the instantaneous flow structure presented Fig. 4 through contours of vorticity. Note that the images vertical displacement of the airfoil in this figure have been exaggerated for viewing clarity. Early in the motion, all resolutions produce virtually the same flow structure; however, just past mid-stroke, the higher spatial resolutions allow an eruption of secondary vortex from the surface that penetrates the leading edge vortex feeding sheet. This secondary vortex pairs with the leading edge vortex, and the structure is propelled away from the surface through self-induction. The added numerical dissipation from the coarsest resolution prevents this eruption from occurring within the time of the motion. Increases spatial refinement also provides a sharper trailing edge vortex, which allows the formation of Kelvin-Helmoltz instabilities in its feeding sheet as it moves into the wake. The added resolution of these features does not appear to affect the integrated quantities as they are not in close enough proximity to the surface.

Tables 4 and 5 provide a listing of the maximum CFL numbers achieved during the motion at each time step for $\text{Re} = 1000$ and 5000 respectively. The local CFL number is computed by

$$CFL_{\text{local}} = \Delta\tau \max \left(J(\Lambda_c^\xi + C\Lambda_v^\xi), J(\Lambda_c^\eta + C\Lambda_v^\eta) \right) \quad (3)$$

where J^{-1} is the inverse Jacobian or local cell area, Λ_c and Λ_v are the inviscid and viscous spectra radii, respectively, with the superscripts, ξ and η , denoting the direction. These quantities are

$$\Lambda_c^\kappa = \left(|u \kappa_x + v \kappa_y| + a \sqrt{\kappa_x^2 + \kappa_y^2} \right) J^{-1} \quad (4)$$

$$\Lambda_v^\kappa = \max \left(\frac{4}{3\rho}, \frac{\gamma}{\rho} \right) \frac{\mu}{\text{Re Pr}} (\kappa_x^2 + \kappa_y^2) J^{-1} \quad (5)$$

for $\kappa = \xi$ or η , and $a = \sqrt{\gamma p / \rho}$ is the local speed of sound. Typically, central discretization schemes utilize a constant coefficient of $C = 4$ as recommended, for example, by Blazek¹⁶ and the references therein. In all cases, the implicit time-integration scheme allows a maximum CFL number several orders of magnitude greater than the $\mathcal{O}(1)$ constraint of explicit schemes.

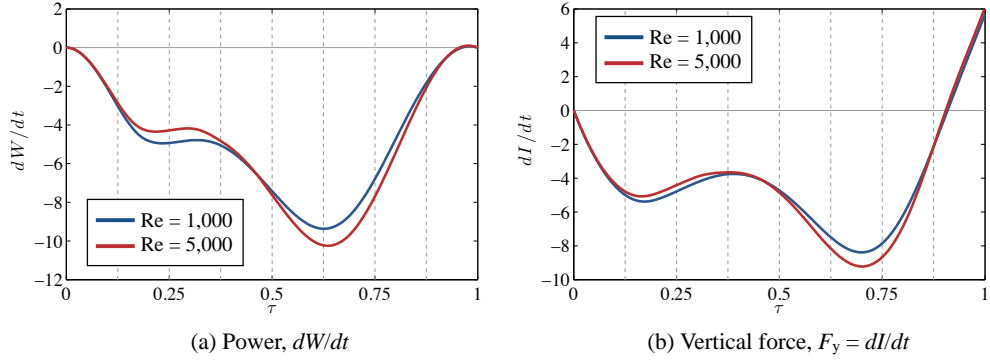


Figure 2: Effect of Reynolds number on the instantaneous power (dW/dt) and vertical force (dI/dt)

Table 2: Effects of temporal and spatial resolutions on work and impulse for $Re = 1000$

$\Delta\tau$	Work			Impulse		
	Coarse	Medium	Fine	Coarse	Medium	Fine
4.00×10^{-3}	-4.84	-4.84	-4.86	-4.31	-4.30	-4.32
2.00×10^{-3}	-4.82	-4.82	-4.82	-4.29	-4.29	-4.30
1.00×10^{-3}	-4.81	-4.81	-4.81	-4.28	-4.29	-4.29
0.50×10^{-3}	-4.80	-4.80	-4.80	-4.28	-4.28	-4.28
0.25×10^{-3}	-4.80	-4.80	-4.80	-4.28	-4.28	-4.28

Table 3: Effects of temporal and spatial resolutions on work and impulse for $Re = 5000$

$\Delta\tau$	Work			Impulse		
	Coarse	Medium	Fine	Coarse	Medium	Fine
4.00×10^{-3}	-4.95	-4.93	-4.94	-4.54	-4.46	-4.48
2.00×10^{-3}	-4.94	-4.95	-4.95	-4.48	-4.38	-4.38
1.00×10^{-3}	-4.93	-4.94	-4.94	-4.46	-4.37	-4.37
0.50×10^{-3}	-4.92	-4.93	-4.94	-4.46	-4.37	-4.37
0.25×10^{-3}	-4.91	-4.93	-4.93	-4.46	-4.36	-4.36

Table 4: Maximum CFL number achieved during the motion for $Re = 1000$

$\Delta\tau$	Coarse	Medium	Fine
4.00×10^{-3}	366	1295	4840
2.00×10^{-3}	186	666	2516
1.00×10^{-3}	93	335	1289
0.50×10^{-3}	47	168	649
0.25×10^{-3}	23	84	325

Table 5: Maximum CFL number achieved during the motion for $Re = 5000$

$\Delta\tau$	Coarse	Medium	Fine
4.00×10^{-3}	129	353	1172
2.00×10^{-3}	64	177	606
1.00×10^{-3}	32	90	308
0.50×10^{-3}	16	46	157
0.25×10^{-3}	8	23	79

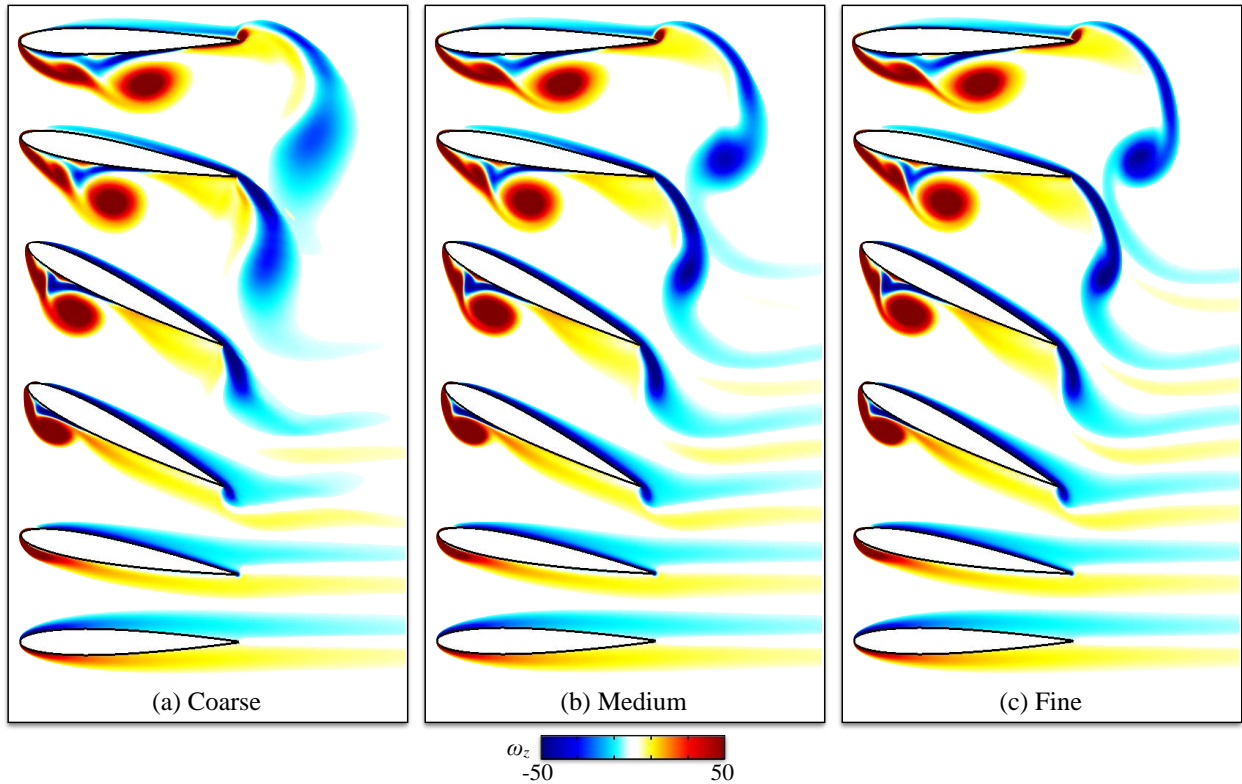


Figure 3: Effect of spatial resolution on the instantaneous flow structure, $Re = 1000$. Note that the heaving displacement has been exaggerated for clarity of the overlaid images.

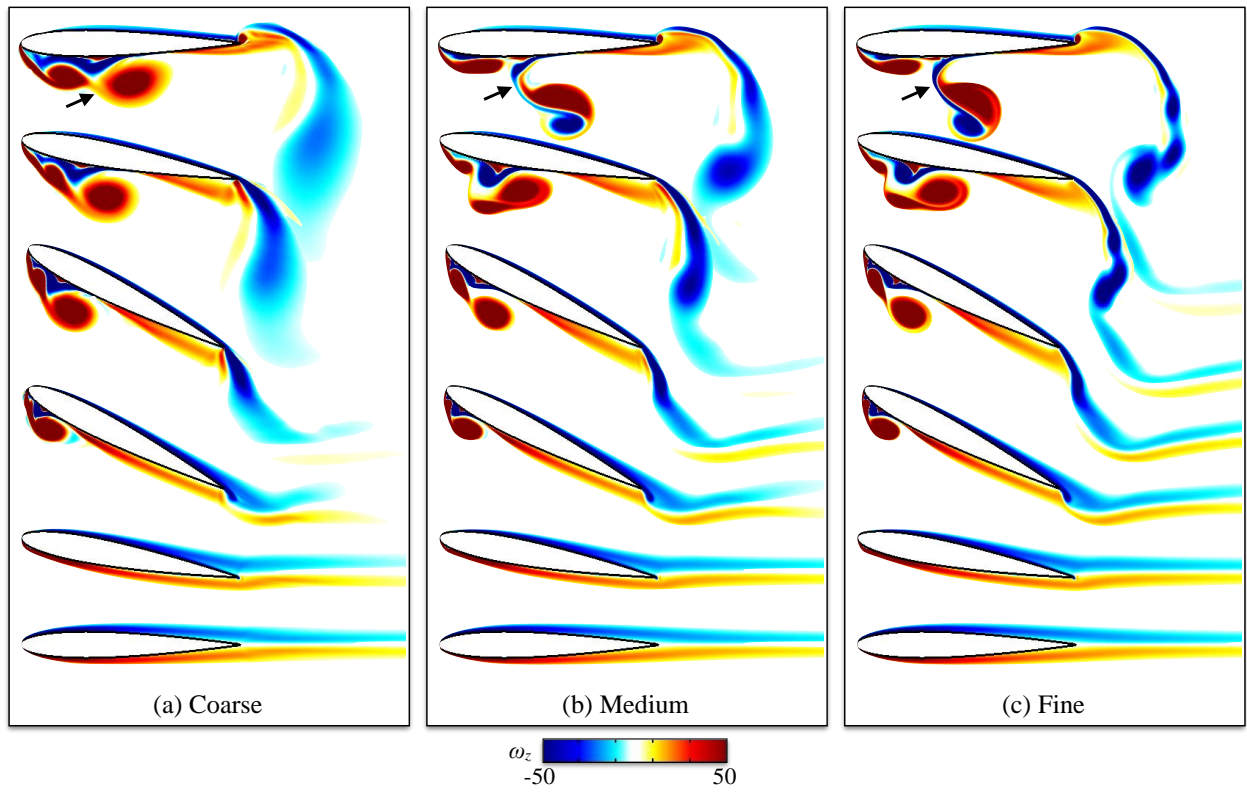


Figure 4: Effect of spatial resolution on the instantaneous flow structure, $Re = 5000$. Note that the heaving displacement has been exaggerated for clarity of the overlaid images.

C3.3: DNS of Taylor-Green Vortex

Case summary

The Taylor-Green vortex field is initialized on the periodic domain, $-\pi \leq (x, y, z) \leq \pi$, with the following:

$$u = \sin(x) \cos(y) \cos(z), \quad (6)$$

$$v = -\cos(x) \cos(y) \cos(z), \quad (7)$$

$$w = 0, \quad (8)$$

$$p = \frac{1}{\gamma M_0^2} + \frac{1}{16} [\cos(2x) + \cos(2y)] [\cos(2z) + 2] \quad (9)$$

$$\rho = \gamma M_0^2 p, \quad (10)$$

where u , v , and w are the Cartesian velocity components, p is the pressure, and ρ is the density. A uniform dimensionless temperature field of unity has been assumed along with the perfect gas relation. The reference Mach number is chosen as $M_0 = 0.1$ in order to minimize effects of compressibility, and the ratio of specific heats is $\gamma = 1.4$. A constant Prandtl number of $\text{Pr} = 0.71$ is also assumed along with Stokes' hypothesis for the bulk viscosity, $\lambda = -2/3 \mu$.

The velocity components have been normalized by the maximum initial speed, V_0 , density is normalized by its initial mean value, ρ_0 , and pressure is nondimensionalized by $\rho_0 V_0^2$, while the spatial components, (x, y, z) , have been scaled by the reference domain length, L . The Reynolds number based on the maximum initial velocity, mean density, and reference length, is $\text{Re} = \rho_0 V_0 L / \mu = 1,600$.

Four meshes with successive refinement of 65, 129, 193, and 257 points in each direction, respectively, are used to discretize the periodic domain. The dimensionless time step for each grid is chosen such that the initial maximum CFL condition is close to unity in order to ensure stability. The higher resolutions are also run in parallel through decomposition of the domain into a number of MPI processes. Details of each mesh including the dimensions, corresponding time step, maximum CFL, and number of processors are listed in Table 6.

Table 6: Mesh and simulation details

N	Time step	CFL_{max}	Processors
65	5.00×10^{-3}	0.933	1
129	2.50×10^{-3}	0.933	8
193	1.60×10^{-3}	0.896	27
257	1.25×10^{-3}	0.933	64

Each simulation of the Taylor-Green vortex decay was run for 20 convective times, $\tau = t V_0 / L$, and several integrated quantities were computed and saved each time step. These quantities include the dimensionless kinetic energy,

$$E_k = \frac{1}{\Omega} \int_{\Omega} \frac{1}{2} \rho (\mathbf{v} \cdot \mathbf{v}) d\Omega, \quad (11)$$

the enstrophy,

$$\epsilon = \frac{1}{\Omega} \int_{\Omega} \frac{1}{2} \rho (\boldsymbol{\omega} \cdot \boldsymbol{\omega}) d\Omega, \quad (12)$$

the viscous dissipation rate,

$$\epsilon_1 = \frac{1}{\Omega \text{Re}} \int_{\Omega} 2(\mathbf{S}^d : \mathbf{S}^d) d\Omega, \quad (13)$$

and the pressure diffusion rate,

$$\epsilon_3 = -\frac{1}{\Omega} \int_{\Omega} p(\nabla \cdot \mathbf{v}) d\Omega, \quad (14)$$

where $\Omega = (2\pi)^3$ is the domain volume, \mathbf{v} is the velocity vector, $\boldsymbol{\omega} = \nabla \times \mathbf{v}$ is the vorticity vector, and \mathbf{S}^d is the deviatoric part of the rate of strain tensor given by

$$S_{ij}^d = \frac{1}{2} \left(\frac{\partial u_i}{\partial x_j} + \frac{\partial u_j}{\partial x_i} \right) - \delta_{ij} \frac{1}{3} \frac{\partial u_k}{\partial x_k} \quad (15)$$

Expanding the inner product of $2(\mathbf{S}^d : \mathbf{S}^d)$ and recombining terms, we are left with the viscous dissipation function:

$$2(\mathbf{S}^d : \mathbf{S}^d) = \left[2 \left(\frac{\partial u}{\partial x} \right)^2 + 2 \left(\frac{\partial v}{\partial y} \right)^2 + 2 \left(\frac{\partial w}{\partial z} \right)^2 + \left(\frac{\partial v}{\partial x} + \frac{\partial u}{\partial y} \right)^2 + \left(\frac{\partial w}{\partial y} + \frac{\partial v}{\partial z} \right)^2 + \left(\frac{\partial u}{\partial z} + \frac{\partial w}{\partial x} \right)^2 - \frac{2}{3} \left(\frac{\partial u}{\partial x} + \frac{\partial v}{\partial y} + \frac{\partial w}{\partial z} \right)^2 \right] \quad (16)$$

All derivatives of the high-order solution are computed with sixth-order, compact finite-differences. Integrations over the periodic domain of a generic integrand, ϕ , are computed through trapezoidal integration, which reduces to

$$\frac{1}{\Omega} \int_{\Omega} \phi d\Omega = \frac{1}{(2\pi)^3} \sum_{i,j,k=1}^{N-1} \phi_{i,j,k} J_{i,j,k}^{-1} \quad (17)$$

where $J = \partial(\xi, \eta, \zeta)/\partial(x, y, z)$ is the Jacobian of the transformation from Cartesian to computational coordinates, and N is the number of grid points in each direction. In the case of a uniform grid on a domain of length, 2π , the inverse Jacobian is constant, $J_{i,j,k}^{-1} = \Delta x \Delta y \Delta z = (2\pi/(N-1))^3$

Results

The temporal evolution of the integrated kinetic energy, E_k , is shown in Fig. 5 for the spatial resolutions described in the previous section along with the supplied reference data from a pseudo-spectral incompressible flow solver computed with 512^3 degrees of freedom. Resolutions with $N > 65$ provide nearly identical kinetic energy over the simulation time. The mesh with $N = 65$ decays slightly ahead of the other spatial resolutions. This is shown more clearly in the evolution of the time rate-of-change of the kinetic energy, $-dE_k/dt$, displayed in Fig. 6(a), where $N = 65$ produces a similar decay rate but with the peak value occurring slightly before the other resolutions. All meshes show slight fluctuations of the decay rates around the peak values that are not identifiable in the spectral result.

Next, the enstrophy is plotted in Fig. 6(b). Increased spatial resolution provides less dissipation and produces higher peak enstrophy that approaches the spectral result with $N = 257$ matching very closely over the entire simulation. Similar distributions of the viscous dissipation rate, ϵ_1 , are seen in Fig. 6(c), indicating that the energy decay rate is dominated by viscous diffusion.

Finally, the pressure diffusion rate, ϵ_3 , is shown in Fig. 6(d) for each spatial resolution. Compressibility effects diminish substantially with spatial resolution with $N > 193$ producing values two orders of magnitude less than the viscous dissipation rates of Fig. 6(c).

Tabulated values for τ , E_k , $-dE_k/d\tau$, ϵ , ϵ_1 , and ϵ_3 are provided for each mesh in the attached files:

- *IntegralValues-N065.dat*
- *IntegralValues-N129.dat*
- *IntegralValues-N193.dat*
- *IntegralValues-N257.dat*

An example format of these files is as follows:

```

      TAU          ENERGY          -dE/dt          ENSTROPY          EPS1          EPS3
5.00000000e-03  1.24997656e-01  4.68601357e-04  3.74447088e-01  4.68742418e-04 -1.51310507e-08
1.00000000e-02  1.24995313e-01  4.68737496e-04  3.74443022e-01  4.68737296e-04 -4.25411833e-08
1.50000000e-02  1.24992969e-01  4.68620032e-04  3.74440926e-01  4.68734620e-04 -1.06303334e-07
2.00000000e-02  1.24990627e-01  4.68462946e-04  3.74440799e-01  4.68734406e-04 -2.23483044e-07
2.50000000e-02  1.24988285e-01  4.68252098e-04  3.74442641e-01  4.68736653e-04 -4.02306290e-07
      ...          ...          ...          ...          ...          ...

```

All computations were performed on an in-house cluster at AFRL consisting of 2.67 GHz Intel X5650 Westmere processors and 2.6 GHz Intel E5 Sandy Bridge processors with 2 GB of RAM per core and connectivity maintained through an 8x Infiniband network interconnect. The computational cost of *FDL3DI* for each mesh on this system is documented in Table 7. The work units are normalized by the runtime of the timing code, TauBench, run on one processor with 250,000 points for 10 pseudo-times. This yielded a normalization time of $T = 9.073$ sec. The total work units increase with resolution since the time-step decreases, and therefore, more iterations are required to simulate 20 convective times. Additionally, the mesh with $N = 193$ resulted in higher work units per iteration than the other cases due to poor load balancing on the system.

Table 7: Computational cost

N	Processors	Iterations	Time/Iter. [sec]	Work Units/Iter.	Total Work Units
65	1	4,000	2.527	0.279	1,114
129	8	8,000	3.663	0.404	3,230
193	27	12,500	5.756	0.634	7,930
257	64	16,000	3.685	0.406	6,499

TauBench normalization time computed over 10 pseudo-times
on one processor with 250,000 points, $T = 9.073$ sec

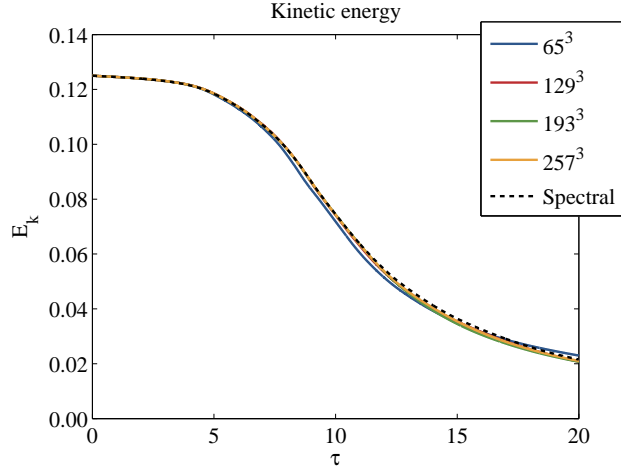


Figure 5: Temporal evolution of the kinetic energy

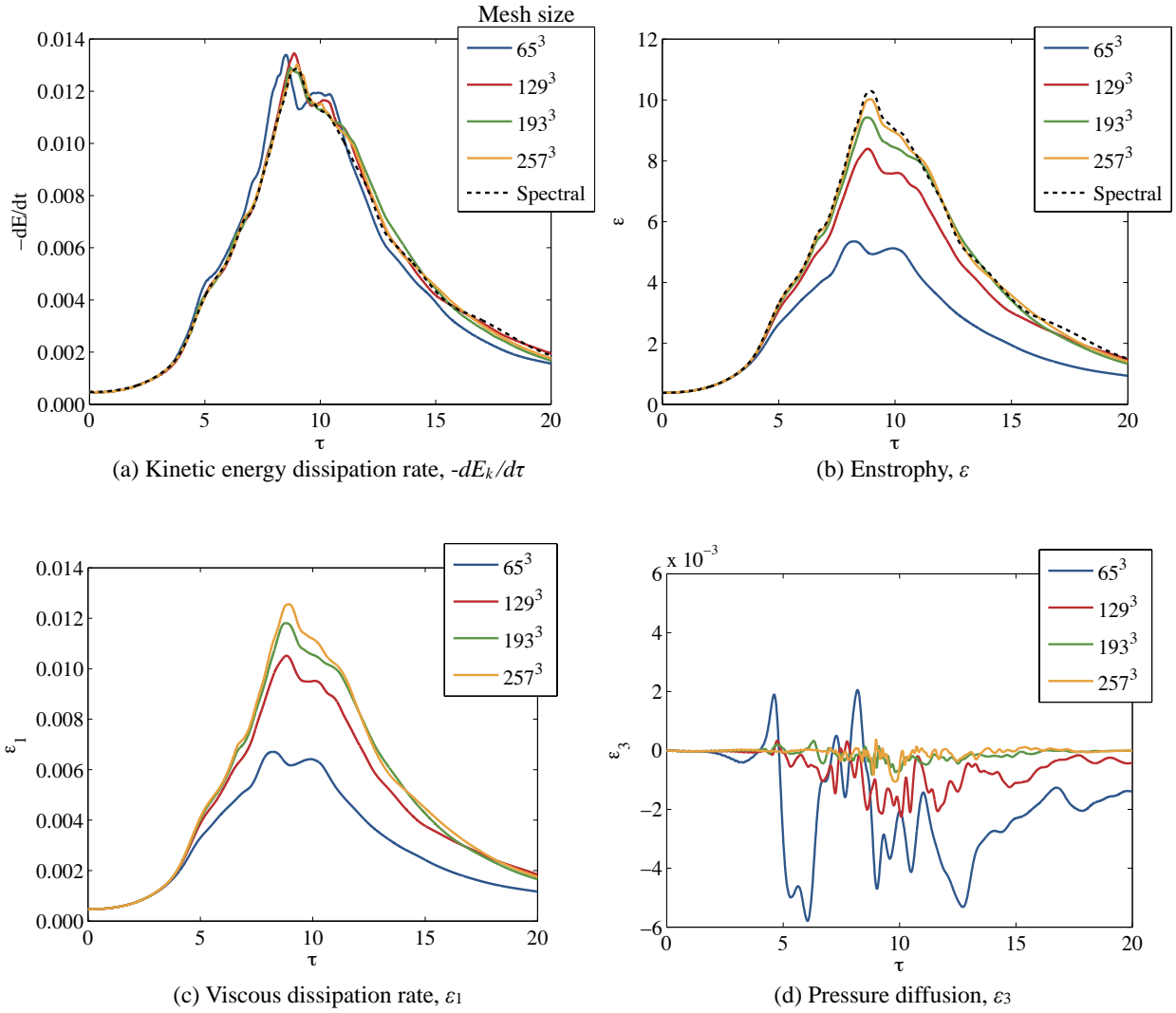


Figure 6: Temporal evolution of the (a) kinetic energy dissipation rate, (b) entropy, (c) viscous dissipation, and (d) pressure diffusion

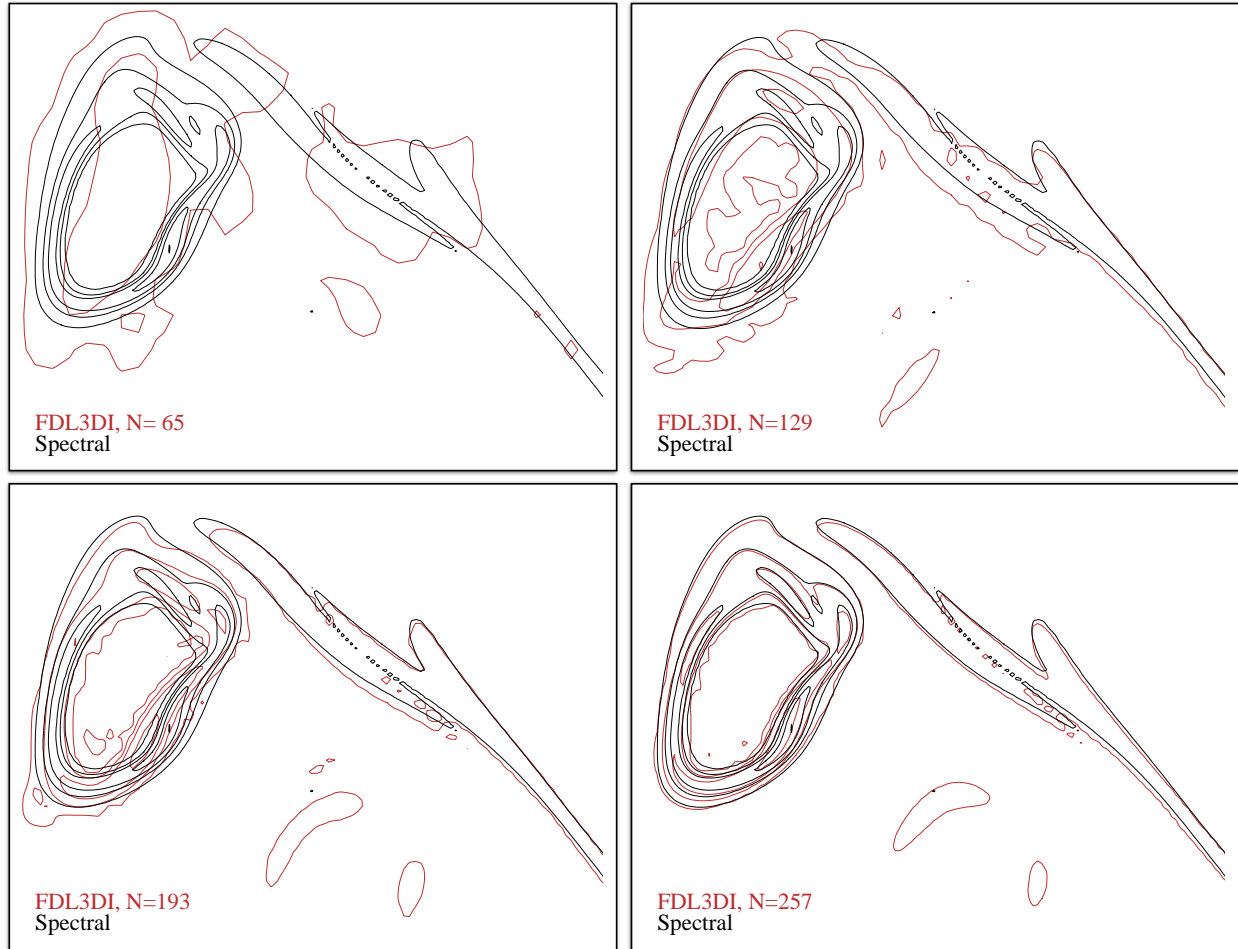


Figure 7: Computed contours of vorticity ($|\omega|L/V_0 = 1, 5, 10, 20, 30$) on a subset of the periodic face, $x/L = -\pi$ at time $t/t_c = 8$. Results from the a pseudo-spectral code are also overlaid for comparison.

C3.4: DNS and LES of Flow over a 2D Periodic Hill

Case summary

Large-Eddy simulations are conducted of flow over a streamwise-periodic hill for two Reynolds numbers, $Re_b = 2800$ and 10595 . The preferred source term for driving a constant mass flow through the channel that was outlined in the case description led to spurious and persistent acoustic perturbations in the evolving solution that dramatically affected the bulk fluid. The recommended source term based on the inlet plane quantities and a simplified momentum equation is believed to be ill-posed for high-order, compressible solvers. For this reason, a source term has been adopted based on the work of Ziefle *et al.*¹⁷. In their work, the constant mass flow is driven by a temporally varying but spatially constant source term added to the streamwise momentum equation designed to enforce a constant volume-integrated streamwise momentum, enforced as

$$\frac{\partial}{\partial t} \int_{\mathcal{V}} \rho u \, dV = \int_{\mathcal{V}} \text{RHS}_{\rho u} \, dV + \beta \int_{\mathcal{V}} dV \equiv 0 \quad (18)$$

where $\text{RHS}_{\rho u}$ is the right-hand side of the streamwise momentum equation including all convective and viscous components. Integration is taken over the entire computational domain, \mathcal{V} . The forcing term, β , is computed at each instant of the evolving solution and is also added to the energy equation in the form, βu . This requires renormalization of all flow variables in terms of the volume-integrated Reynolds number ($Re_{\mathcal{V}}$), which relates geometrically to the hill crest normalization¹⁷ by

$$Re_{\mathcal{V}} \approx 0.72 Re_b \quad (19)$$

leading to Reynolds numbers of $Re_{\mathcal{V}} = 2016$ and 7628 to achieve the proper hill crest Reynolds numbers of $Re_b = 2800$ and 10595 , respectively, as indicated in the case description. The Mach number should also be scaled for consistency; however, this quantity had been unintentionally neglected at the beginning of the study, so $M_{\mathcal{V}} = 0.1$ leading to $M_b \approx 0.139$ for all cases presented below. Implementation of this source term resulted in a well-behaved, evolving solution without spurious waves.

Results

Three spatial resolutions have been considered for this study, and each are listed in Table 8 along with the corresponding mean streamwise, normal, and spanwise spacings at the lower wall. The coarse mesh, for example, is prescribed with 129 gridlines in the streamwise direction, 65 gridlines in the normal direction, and 65 gridlines equally distributed in the spanwise direction. The medium and fine resolutions are 2 and 4 times refined, respectively, in each direction from the coarse mesh. A depiction of the geometry and discretization is shown in Fig. 8 for the coarse resolution where every other gridline is shown for clarity. The grids used throughout this study do not correspond to those provided by the case organizer since those did not enforce normal gridlines at the solid surfaces, which may not be required for a finite volume or element method, but could cause errors in the boundary condition approximations with a finite difference scheme.

The top and bottom boundaries are prescribed as no-slip walls with a zero-normal pressure gradient that is approximated by a third-order accurate extrapolation, while the streamwise and spanwise boundaries are periodic. All simulations utilize a nondimensional time step of $\Delta\tau = 0.001$ with the second-order, implicit time-integration scheme outlined in the introduction. The coarse mesh is initialized with a parabolic velocity distribution at each x -station that achieves the desired mass flow and is simulated for 50 flow-through lengths of the domain. That solution is then

Table 8: Mean mesh spacings in the normal, streamwise, and spanwise directions for three resolutions

Resolution	$\Delta s/h$	$\Delta n/h$	$\Delta z/h$
$129 \times 65 \times 65$	0.0047	0.0106	0.0703
$257 \times 129 \times 129$	0.0094	0.0053	0.0352
$513 \times 257 \times 257$	0.0188	0.0026	0.0176

$\Delta s/h$ streamwise spacing
 $\Delta n/h$ normal spacing
 $\Delta z/h$ spanwise spacing

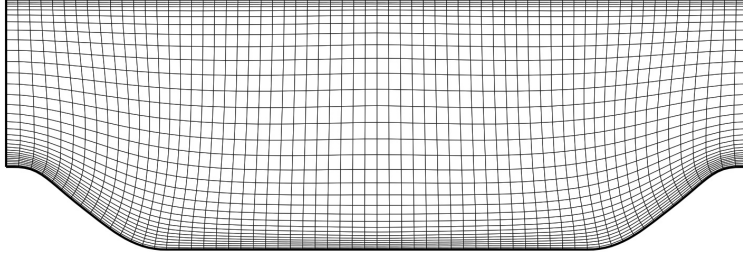


Figure 8: Depiction of the domain at the coarse resolution ($129 \times 65 \times 65$) where every other gridline is shown in each direction for clarity

interpolated onto the medium and fine resolutions, and all are advanced for another 50 flow-through lengths to establish the periodic flow at each resolution, followed by another 50 flow-through lengths of simulation for statistics gathering of the time-mean quantities. The resulting average Reynolds number, mass flow rate, and forcing terms are documented in Tables 9 and 10 for $Re_b = 2800$ and 10595, respectively. The established temporal evolution of the mass flow rate and source term from the medium resolution are shown in Fig. 9 over the last 50 flow-through lengths, and the corresponding time-averaged solution is also depicted in Fig. 10. Here, the time-mean streamlines are shown along with the turbulent kinetic energy in (a) and the velocity profiles at several x -stations in (b). Profiles from DNS results are also overlaid on the computed results from this study, and shown to be in very favorable agreement.

Along with this abstract, several other quantities have been provided to the case organizer in the format requested in the case description. These include the pressure and skin friction distributions along the lower wall of the domain (X-CP-CF.dat), the temporal evolution of the mass flow rate (mass-flow.dat), and profiles of the time-mean and fluctuating quantities: \bar{u}/u_b , \bar{v}/u_b , $\overline{u'u'}/u_b^2$, $\overline{v'v'}/u_b^2$, $\overline{w'w'}/u_b^2$, and $\overline{u'v'}/u_b^2$. The profiles are taken at streamwise stations of $x/h = 0.05, 0.5, 1, 2, 3, 4, 5, 6, 7,$ and 8 measured from the hill crest, which are provided in the files, AVG-PROFILES-01.dat, AVG-PROFILES-02.dat, ..., AVG-PROFILES-10.dat, respectively.

Table 9: Periodic Hill Average Quantities, $Re = 2800$

Resolution	\bar{Re}_b	\bar{m}/A_c	$\bar{\beta}$
$129 \times 65 \times 65$	2797	0.9997	0.0129
$257 \times 129 \times 129$	2796	0.9998	0.0119
$513 \times 257 \times 257$	2796	0.9998	0.0119

Table 10: Periodic Hill Average Quantities, $Re = 10595$

Resolution	\overline{Re}_b	$\overline{\dot{m}/A_c}$	$\overline{\beta}$
$129 \times 65 \times 65$	10590	0.9989	0.0098
$257 \times 129 \times 129$	10583	0.9998	0.0092
$513 \times 257 \times 257$	10581	0.9999	0.0097

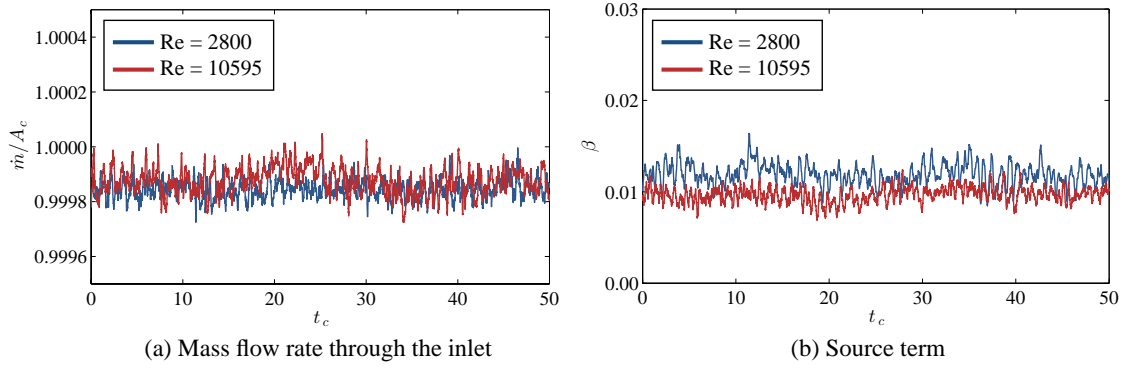


Figure 9: Temporal evolution of (a) the mass flow rate, \dot{m}/A_c , and (b) the source term, β

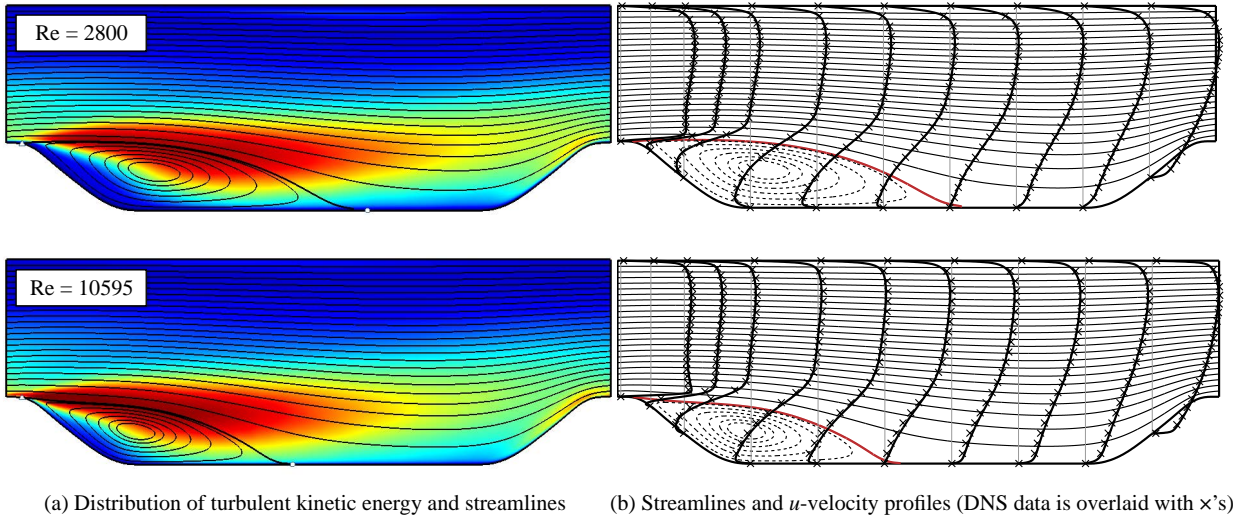


Figure 10: Distribution of turbulent kinetic energy, streamlines, and u -velocity profiles from the time-mean and spanwise averaged solution on the medium resolution; (a) TKE and streamlines, (b) Streamlines and u -velocity profiles along with profiles from available DNS

References

- [1] M.R. Visbal and D.V. Gaitonde. High-order accurate methods for complex unsteady subsonic flows. *AIAA Journal*, 37(10):1231–1239, 1999.
- [2] D. Gaitonde and M. Visbal. High-order schemes for Navier-Stokes equations: Algorithm and implementation into FDL3DI. Technical Report AFRL-VA-WP-TR-1998-3060, Air Force Research Laboratory, Wright-Patterson AFB, 1998.
- [3] S. Lele. Compact finite difference schemes with spectral-like resolution. *Journal of Computational Physics*, 103(1):16–42, 1992.
- [4] M.R. Visbal and D.V. Gaitonde. On the use of high-order finite-difference schemes on curvilinear and deforming meshes. *Journal of Computational Physics*, 181:155–185, 2002.
- [5] D. Gaitonde and M. Visbal. Further development of a Navier-Stokes solution procedure based on higher-order formulas. AIAA Paper 99-0557, AIAA, 1999.
- [6] P. Alpert. Implicit filtering in conjunction with explicit filtering. *Journal of Computational Physics*, 44(1):212–219, 1981.
- [7] M.R. Visbal and D.P. Rizzetta. Large-eddy simulation on curvilinear grids using compact differencing and filtering schemes. *Journal of Fluids Engineering*, 124:836–847, 2002.
- [8] M.R. Visbal, P.E. Morgan, and D.P. Rizzetta. An implicit LES approach based on high-order compact differencing and filtering schemes. AIAA Paper 2003-4098, AIAA, June 2003.
- [9] D. Garmann, M. Visbal, and P. Orkwis. Comparative study of implicit and subgrid-scale model large-eddy simulation techniques for low-Reynolds number airfoil applications. *International Journal for Numerical Methods in Fluids*, 71(12):1546–1565, 2013. doi: 10.1002/fld.3725.
- [10] R. Beam and R. Warming. An implicit factored scheme for the compressible Navier-Stokes equations. *AIAA Journal*, 16(4):393–402, 1978.
- [11] T. Pulliam and D. Chaussee. A diagonal form of an implicit approximate-factorization algorithm. *Journal of Computational Physics*, 17(10):347–363, 1981.
- [12] D.P. Rizzetta, M.R. Visbal, and P.E. Morgan. A high-order compact finite-difference scheme for large-eddy simulation of active flow control (invited). AIAA Paper 2008-526, AIAA, 2008.
- [13] A. Jameson, W. Schmidt, and E. Turkel. Numerical solutions of the euler equations by finite volume methods using runge-kutta time stepping schemes. AIAA Paper 1981-1259, AIAA, 1981.
- [14] T. Pulliam. Artificial dissipation models for the euler equations. *AIAA Journal*, 24(12):1931–1940, Dec. 1986.
- [15] D. J. Fyfe. Economical evaluation of Runge-Kutta formulae. *Mathematics of Computation*, 20(95), 1966.
- [16] J. Blazek. *Computational Fluid Dynamics: Principles and Applications*. Elsevier Science, 2006.
- [17] J. Ziefle, S. Stolz, and L. Kleiser. Large-eddy simulation of separated flow in a channel with streamwise-periodic constrictions. *AIAA Journal*, 47(7):1705–1718, July 2008.